Heterostructures of graphene and nitrogenated holey graphene: Moiré pattern and Dirac ring

Jun Kang,[1,*] Seyda Horzum,[1,2] and François M. Peeters[1]

[1]*Department of Physics, University of Antwerp, Groenenborgerlaan 171, B-2020 Antwerp, Belgium*

[2]*Department of Engineering Physics, Faculty of Engineering, Ankara University, 06100 Ankara, Turkey*

(Received 15 July 2015; revised manuscript received 16 September 2015; published 19 November 2015)

Nitrogenated holey graphene (NHG) is a recently synthesized two-dimensional material. In this paper the structural and electronic properties of heterostructures of graphene and NHG are investigated using first-principles and tight-binding calculations. Due to the lattice mismatch between NHG and graphene, the formation of a moiré pattern is preferred in the graphene/NHG heterostructure, instead of a lattice-coherent structure. In moiré-patterned graphene/NHG, the band gap opening at the K point is negligible, and the linear band dispersion of graphene survives. Applying an electric field modifies the coupling strength between the two atomic layers. The Fermi velocity v_F is reduced as compared to the one of pristine graphene, and its magnitude depends on the twist angle θ between graphene and NHG: For $\theta = 0^\circ$, v_F is 30% of that of graphene, and it increases rapidly to a value of 80% with increasing θ. The heterostructure exhibits electron-hole asymmetry in v_F, which is large for small θ. In NHG encapsulated between two graphene layers, a "Dirac ring" appears around the K point. Its presence is robust with respect to the relative stacking of the two graphene layers. These findings can be useful for future applications of graphene/NHG heterostructures.

DOI: 10.1103/PhysRevB.92.195419 PACS number(s): 61.46.−w, 73.22.Pr, 71.15.Mb

I. INTRODUCTION

Graphene is known for its structural stability and extraordinary electronic and thermal conductivity [1,2]. However, the lack of an energy band gap limits its use in field-effect and optoelectronic devices. A search for novel semiconducting ultrathin compounds that share some of graphene's features is highly needed. Recent experimental and theoretical studies have demonstrated that vacancy or adatom engineered graphenes are promising candidates for switchable and high mobility electron transport applications [3–5]. In addition, another method to form a graphene variant is by creating two-dimensional polymers in which graphenelike building blocks are linked to each other by strong covalent bonds and linker atom groups [6–9]. Very recently, Mahmood *et al.*, demonstrated experimentally that the formation of a large area of a nitrogenated holey graphene (NHG) structure can be realized easily using the wet-chemistry-based bottom-up approach [10]. NHG crystal has a strictly two-dimensional atomic structure, and it exhibits exceptionally high crystal and electronic quality, along with a considerable band gap of 1.96 eV. In addition, studies revealed its possibility for hydrogen purification [11], hydrogen evolution [12], and water splitting [13].

Stacking different 2D monolayers together results in so-called van der Waals heterostructures [14]. Such heterostructures have atomic sharp interfaces without dangling bonds and exhibit many novel properties that are potentially interesting for applications. For example, long-lived interlayer excitons are observed in $MoSe_2/WSe_2$ heterostructure [15]. Atomically thin p-n junctions [16] and light-emitting diodes [17] have been realized using van der Waals heterostructure. The properties of graphene can also change greatly by constructing van der Waals heterostructures with different materials. Localized Dirac fermions are predicted to appear in twisted bilayer graphene [18], and cloning of Dirac cones [19] is observed in a graphene/BN heterostructure. Since NHG is a newly synthesized 2D material, it is interesting to explore the structural and electronic properties of graphene/NHG (G/NHG) van der Waals heterostructures and investigate how the Dirac fermion of graphene is affected in the heterostructure.

In this paper, we study the structural and electronic properties of heterostructures of graphene and NHG. After the introduction the rest of the paper is organized as follows: Computational methodology is given in Sec. II. The properties of monolayer NHG are briefly introduced in Sec. III. In Sec. IV bilayer G/NHG heterostructures are discussed, including its atomic structure, the band structure, effects of a perpendicular electric field, and the renormalized Fermi velocity. Finally the band structure of NHG encapsulated between two graphene layers is investigated in Sec. V. Our conclusions are given in Sec. VI.

II. COMPUTATIONAL METHODOLOGY

For geometry optimization and the determination of the electronic structure of NHGs we performed first-principles calculations within the density functional theory (DFT) using the plane-wave projector-augmented wave (PAW) method [20] as implemented in the Vienna *ab initio* simulation package (VASP) [21,22]. The Perdew-Burke-Ernzerhof (PBE) [23] form of the generalized gradient approximation (GGA) was adopted to describe electron exchange and correlation. The kinetic energy cutoff for the plane-wave expansion was set to 400 eV where the hexagonal Brillouin zone (BZ) was sampled with a Γ-centered $7 \times 7 \times 1$ k-point grid. To avoid interaction between adjacent NHG sheets, we put a large vacuum spacing of 15 Å in the perpendicular direction. The convergence threshold for energy was chosen as 10^{-5} eV and 10^{-2} eV/Å for the force. For the calculation of the density of states, the tetrahedron method with Blöchl corrections is used. The charge distribution on the atoms was calculated using the Bader analysis [24,25]. The effect of van der Waals

*jun.kang@uantwerpen.be

interaction was included by using the empirical correction scheme of Grimme [26].

For large scale moiré pattern structure calculations, we employed a tight-binding (TB) model. We limited studies to the p_z orbital for both C and N atoms, since we are mainly interested in the states around the Fermi level which are all p_z orbitals. The Hamiltonian has the form [27]:

$$H = \sum_i \epsilon_i |i\rangle\langle i| + \sum_{i\neq j} t_{ij} |i\rangle\langle j|, \quad (1)$$

where $|i\rangle$ is the p_z orbital of the atom located at $\vec{r}_i$, ϵ_i is the onsite energy, and t_{ij} is the coupling parameter. In monolayer graphene, only the $pp\pi$ interaction is relevant, but in the graphene/NHG heterostructure, both $pp\pi$ and $pp\sigma$ interactions are important. According to the Slater-Koster formula [28], t_{ij} is given by:

$$t_{ij} = n^2 V_{pp\sigma}(r_{ij}) + (1-n^2) V_{pp\pi}(r_{ij}), \quad (2)$$

where n is the direction cosine along the z direction of the vector $\vec{r}_j - \vec{r}_i = \vec{r}_{ij}$, and $r_{ij} = |\vec{r}_{ij}|$. The functions $V_{pp\pi}$ and $V_{pp\sigma}$ are assumed to have the form $\gamma e^{q(1-r_{ij}/a)}$. More details about the model and the fitting parameters γ, q, a, and ϵ_i are given in the Appendix. Our tests show that the model can well reproduce the VASP results.

III. SINGLE LAYER CRYSTAL STRUCTURE OF NHG

The primitive unit cell of the NHG crystal structure, with the formula C_2N, can be constructed using two benzene rings surrounded by six nitrogen atoms. As shown in Fig. 1(a), in NHG carbon and nitrogen atoms form a 18-atomic hexagonal unit cell with the lattice constant 8.29 Å. Similar to graphene, the strong sp^2 hybridization between carbon and nitrogen atoms leads to the formation of an atomically flat holey structure. In addition NHG structure contains three types of bond lengths; 1.33 Å for carbon-nitrogen bonds, 1.46 Å for carbon-carbon bonds facing the holey side, and 1.43 Å for carbon-carbon bonds located in between the nitrogen linkers. It appears from the short bond lengths that, withstanding the presence of the nitrogen atoms between the benzene rings, the NHG crystal structure is quite stable. According to our Bader charge analysis, the holey site of graphene is surrounded by negatively charged N atoms ($-1.1\ e$), while each C atom in the benzene rings donates about 0.55 e. However, strong carbon-nitrogen hybridization leads to the emergence of some additional features such as an energy band gap. The band structure of the NHG monolayer is shown in Fig. 1(b). It has a direct band gap located at the Γ point. Around the band edges there are several flat bands. The contour plots of the lowest conduction band (CB) and highest valence band (VB) around the Γ point are presented in Figs. 1(c) and 1(d). Notice that the CB exhibits a much more anisotropic behavior than the VB. From Figs. 1(c) and 1(d) it is seen that the contour lines for VB are more circlelike than those for the CB. The energy changes from Γ to K and from Γ to M are 0.08 eV and 0.11 eV for VB, respectively. But for CB, the values are 0.76 eV and 0.06 eV. The PBE predicted energy gap value is 1.65 eV at the Γ point, which is smaller than the experimental value of 1.96 eV, due to the well known band gap underestimation of PBE. These results are in good agreement with those reported by Zhang *et al.* [29]. The PBE-predicted effective masses are $17.25m_0$ for the hole and $1.13m_0$ for the electron along Γ-K and $22.34m_0$ for the hole and $2.77m_0$ for the electron along Γ-M, where m_0 is the mass of a free electron.

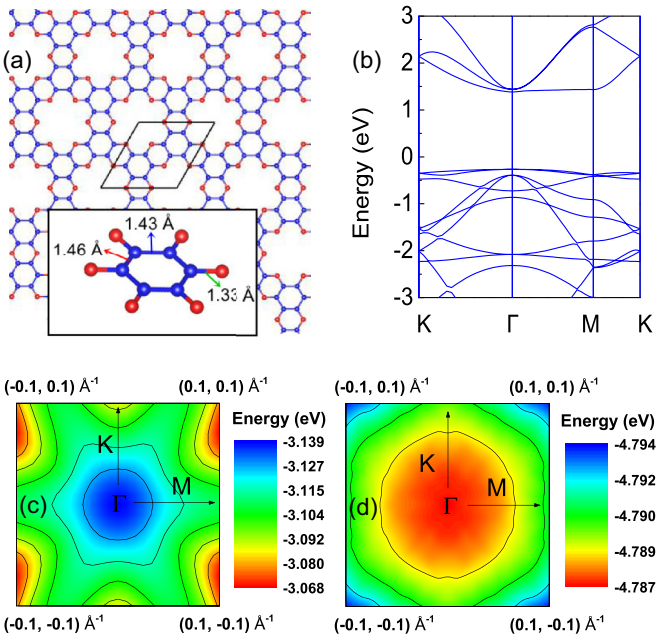

FIG. 1. (Color online) (a) Top view of the atomic structure of a single layer holey graphene. Nitrogen and carbon atoms are shown by red and blue balls, respectively. Primitive unit cell of the crystal is delineated by black rhombus. Tilted perspective view of a N-surrounded benzene unit and bond lengths are given in the inset. (b) Band structure of NHG monolayer. (c) Contour plot of the lowest conduction band around the Γ point. (d) The same as (c) but for the highest valence band.

IV. BILAYER HETEROSTRUCTURES OF GRAPHENE AND NHG

A. Atomic structure: Ordered stacking versus moiré pattern

First we briefly describe the construction of the G/NHG heterostructure. The two in-plane primitive lattice vectors of graphene are chosen as $\vec{a}_1 = (1,0)a_0^G$ and $\vec{b}_1 = (\frac{1}{2}, \frac{\sqrt{3}}{2})a_0^G$. For NHG, the primitive lattice vectors are $\vec{a}_2 = (\frac{\sqrt{3}}{2}, -\frac{1}{2})a_0^N$ and $\vec{b}_2 = (\frac{\sqrt{3}}{2}, \frac{1}{2})a_0^N$. Here $a_0^G = 2.46$ Å and $a_0^N = 8.29$ Å are the optimized lattice constants of graphene and NHG. When integers (m,n) and (p,q) meet the condition $|m\vec{a}_1 + n\vec{b}_1| \approx |p\vec{a}_2 + q\vec{b}_2|$, a G/NHG heterostructure can be constructed, with its two lattice vectors being $m\vec{a}_1 + n\vec{b}_1 \approx p\vec{a}_2 + q\vec{b}_2$ and $-n\vec{a}_1 + (m+n)\vec{b}_1 \approx -p\vec{a}_2 + (p+q)\vec{b}_2$. We denote it as (m,n)-(p,q) stacking. Because the lattice of NHG can also be viewed as a honeycomb structure with some missing hexagonal rings, it also has zigzag and armchair directions like graphene. Therefore, one can define the relative twist angle θ in a (m,n)-(p,q)-G/NHG as the angle between the zigzag (or armchair) directions of the NHG layer and the graphene layer. Based on the above defined lattice vectors, the cosine of θ can

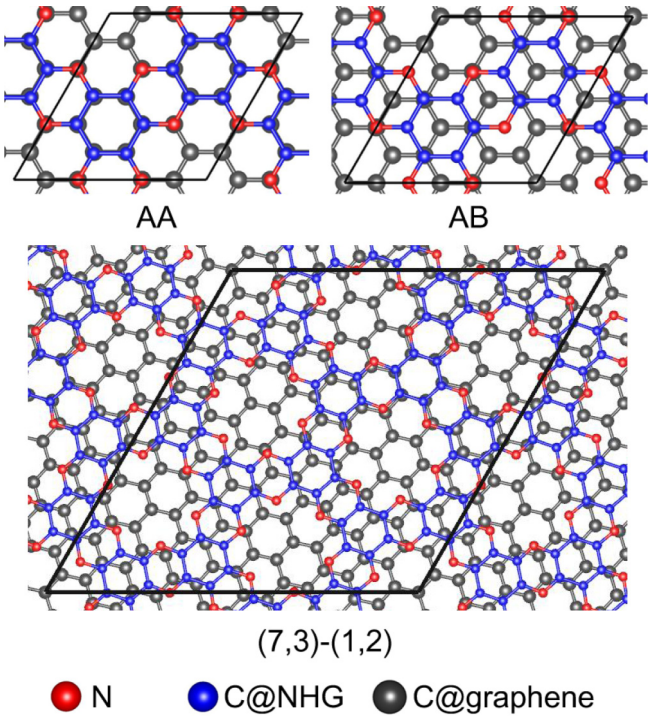

FIG. 2. (Color online) Illustration of the G/NHG heterostructures with AA, AB, and (7,3)-(1,2) stacking. The boxes defined by the solid lines indicate the supercell.

be calculated as:

$$\cos\theta = \frac{\sqrt{3}(mp + mq + nq)}{2\sqrt{(m^2 + mn + n^2)(p^2 + pq + q^2)}}. \quad (3)$$

As NHG has a holey honeycomb lattice, one may expect that, similar to bilayer graphene, the G/NHG heterostructure can exhibit different favorable stacking configurations such as the AA or AB stacking shown in Fig. 2. Regarding the notation described above, AA stacking corresponds to (2,−2)-(1,0)-G/NHG with $\theta = 0^\circ$, and AB stacking corresponds to (2,2)-(1,0)-G/NHG with $\theta = 60^\circ$. In these cases, the lattice mismatch between the graphene layer and the NHG layer is about 3%. Formation of a lattice-matched structure imposes strain to the monolayers, causing extra strain energy. Except for the ordered stacking, another possibility is the formation of a moiré pattern, in which the lattice mismatch between the two constitute layers is maintained, as observed in graphene/BN heterostructures [19,30,31]. In Fig. 2 we show an example of such a moiré pattern, namely the (7,3)-(1,2)-G/NHG. Here the lattice mismatch is less than 0.5%, and the strain energy is negligible. The relative twist angle for this structure is 6.10°. In all these stacking configurations graphene and NHG crystals maintain their planar crystal structure. The interlayer distance is calculated to be 3.36 Å, 3.15 Å, and 3.25 Å for AA, AB, and (7,3)-(1,2) stacking, respectively. Whether the ordered stacking or the moiré pattern is more stable depends on the competition between the interlayer binding energy and the strain energy [32].

The interlayer binding energy is defined by $E_b = (E_{\text{tot}} - E_G - E_{\text{NHG}})/S$, where E_{tot} and S are the total energy and the area of the heterostructure supercell, and E_G and E_{NHG} are the energies of isolated graphene and NHG layers with the same lattice constant as the heterostructure, respectively. The strain energy is calculated by $E_s = (E_G + E_{\text{NHG}} - E_G^0 - E_{\text{NHG}}^0)/S$, where E_G^0 and E_{NHG}^0 are the energies of graphene and NHG layers at their equilibrium state. For different structures, the one with the lowest $E_b + E_s$ is the most stable. For AA, AB, and (7,3)-(1,2) stacking, the interlayer binding energies are −13.41 meV/Å^2, −16.52 meV/Å^2, and −15.27 meV/Å^2, respectively. On the other hand, the strain energy is 5.68 meV/Å^2 for AA and AB stacking, but only about 0.1 meV/Å^2 for the (7,3)-(1,2) stacking. Overall, the $E_b + E_s$ for (7,3)-(1,2) stacking is the lowest. Although AB stacking has the largest gain in the interlayer binding energy, it is compensated by the high strain energy. Therefore, in graphene/NHG heterostructures, a lattice mismatch will be maintained, and the formation of moiré patterns, such as the (7,3)-(1,2) structure, is favored over AA and AB stacking.

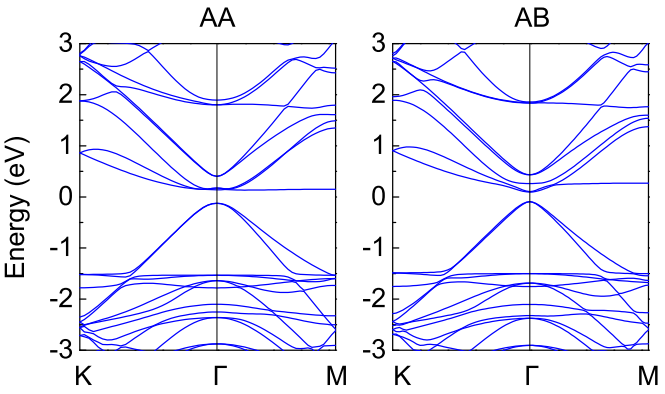

FIG. 3. (Color online) Band structure of the G/NHG heterostructures with AA and AB stacking. The Fermi level is set to zero.

B. Band structure

As the formation of moiré patterns is more favorable, we take the (7,3)-(1,2) structure as an example to discuss the band structure of G/NHG. Although the AA and AB G/NHG are not the ground state (they can possibly be metastable configurations), to see the effect of ordered stacking we first look at their band structures, as shown in Fig. 3. Due to the Brillouin zone folding, the K point of graphene is folded into the Γ point in these structures. Both structures show a band gap opening at the Γ point. The band gap is 0.26 eV for AA stacking and 0.19 eV for AB stacking.

However, the situation for the (7,3)-(1,2) structure is very different, as seen in Fig. 4(a). A linear band dispersion is observed around the K point, with only a negligible band gap opening of 0.3 meV. The bands around the K point are also found to be isotropic. Therefore, the Dirac-fermion-like behavior of carriers in graphene is preserved in G/NHG moiré structures. The qualitative differences in the ordered stacking and the moiré structures can be understood as follows. The AA and AB structures are both commensurate states, in which the graphene lattice follows the periodic potential U created by the NHG layer. This potential results in the scattering between states at $\vec{k}$ and $\vec{k} - \vec{G}$ in the graphene layer, where $\vec{G}$ is the reciprocal lattice vector of U, and the strength depends on

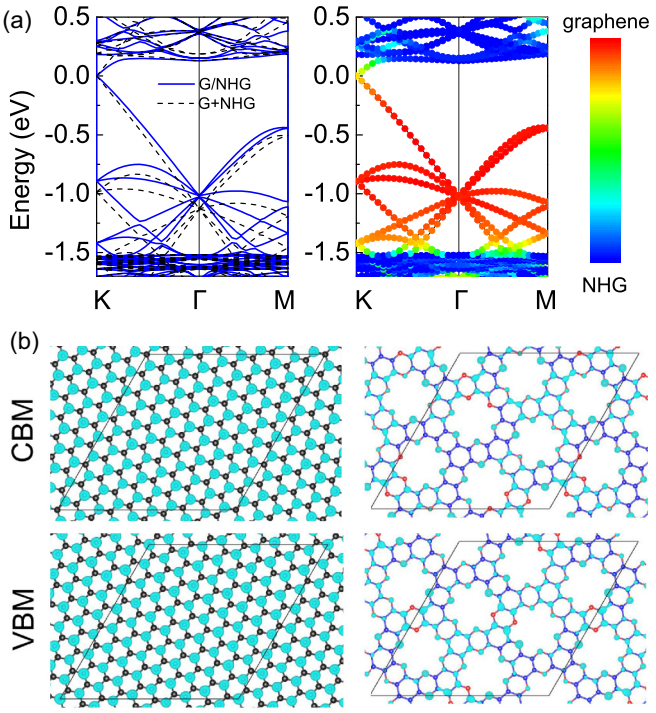

FIG. 4. (Color online) (a) In the left panel, the solid lines indicate band structure of the (7,3)-(1,2) structure (G/NHG), and the dashed lines are the overlap of the bands of isolated graphene and NHG layers (G + NHG). In the right panel the layer projection is given. Blue and red denote the contribution from the NHG and graphene layers, respectively. (b) The partial charge density of the VBM and CBM states at the K point. Left and right panels show the distribution in the graphene and NHG layers, respectively. The isosurface corresponds to 0.00035 e/Å^3.

the $\vec{G}$ Fourier components of U [33]. In the commensurate state, $\vec{G}$ is also the reciprocal lattice vector of the primitive graphene cell. This causes scattering between states at the K point and the K–$\vec{G}$ point, namely between the two Dirac cones. So there will be coupling between the VBM state at one cone and the CBM at the other [33], and consequently the CBM and the VBM are no longer degenerate, leading to the opening of a band gap. In the moiré structures, the lattice periodicity of graphene and NHG (thus the potential U) are incommensurate. In this case $\vec{G}$ is not a reciprocal lattice vector of graphene, and scattering between different Dirac cones doesn't occur. Hence the VBM and CBM states at the K point remain degenerate, and there is no band gap opening. Note that in practical calculations of moiré structures, due to the periodic boundary condition used, graphene and NHG share the same supercell and some $\vec{G}$ may also be the reciprocal lattice vector of graphene. However, the Fourier components of U at these $\vec{G}$ is rather small because they correspond to high frequency contributions. Therefore, the scattering between Dirac cones, and the resulting band gap opening, will be negligible. A similar effect is also predicted for graphene/BN heterostructures. In graphene/BN with a commensurate lattice (such as AA or AB stacking), there is a significant band gap opening [34,35], whereas in graphene/BN heterostructures with a moiré pattern [32,36], the band gap is zero.

Although the van der Waals interaction between graphene and NHG is not strong, it can have a significant influence on the band structure of G/NHG. The interaction introduces a dipole moment which leads to an energy shift between the two layers. According to our calculations, the work function of an isolated graphene layer is 4.24 eV, whereas the electron affinity of an isolated NHG layer is 4.41 eV. In other words, the CBM of NHG is 0.17 eV lower than the Dirac point of graphene. If there is no interaction between graphene and NHG, when they are stacked together the Dirac point of graphene will be buried inside the conduction bands of NHG. However, due to the interlayer coupling, there is charge transfer from graphene to NHG, resulting in a dipole moment. This dipole moment moves up the energy of the NHG layer with respect to the graphene layer. Consequently, in G/NHG the Dirac point of the graphene layer appears inside the band gap of the NHG layer, as shown in Fig. 4(a). In Fig. 4(a) we also show the overlap of the bands of isolated graphene and NHG layers (G + NHG), and the energy shift caused by the dipole moment is included. Comparing the bands of G/NHG and G + NHG, it is found that the general shape of the bands are similar, but the slope of the linear bands around the K point is reduced in the G/NHG. This suggests a renormalization of Fermi velocity caused by the interlayer coupling, which we will discuss in detail in Sec. IV D.

To further show the interlayer coupling effect, the projected weights of the graphene and NHG layers to the electron wave function at a given k point and band state are denoted by different colors in Fig. 4(a). The flat bands of the NHG layer appear at $E > 0.1$ eV and $E < -1.5$ eV. Within the range -1.5 eV $< E < 0.1$ eV, the bands originate mostly from the graphene layer. However, around the Fermi level, strong interlayer coupling is observed. It can be seen that the states close to the K point around 0 eV are not only from the graphene layer but also from the NHG layer. Hence, the Dirac states are distributed not only in the graphene layer but also in the NHG layer. In Fig. 4(b) the charge density of the VBM and CBM states at the K point are shown. These states have a p_z character. In the graphene layer, the VBM and CBM are distributed on different sublattices. Both states also have significant components in the NHG layer. Monolayer NHG is a semiconductor with a considerable band gap. As a consequence of the formation of a moiré heterostructure with graphene, the interlayer coupling brings Dirac-Fermion-like carriers to the semiconducting NHG layer.

C. Effect of electric field

In this part we investigate the effect of an external perpendicular electric field E_{ext} on the band structure of the (7,3)-(1,2) G/NHG. Electric fields of 0.2 V/Å are applied along the $+z$ and $-z$ directions, which are perpendicular to the layer plane. Previously it was demonstrated that the application of an electric field could open a considerable band gap in bilayer graphene [37]. In Fig. 5(a) the band structures and the layer-projected weights of the (7,3)-(1,2) G/NHG under an electric field are plotted. Different from bilayer graphene, the band gap opening induced by the field is still negligible. The gap is only 0.2 meV for $E_{\text{ext}} = 0.2$ V/Å and 0.5 meV for $E_{\text{ext}} = -0.2$ V/Å. Hence, in practice the Dirac cone can

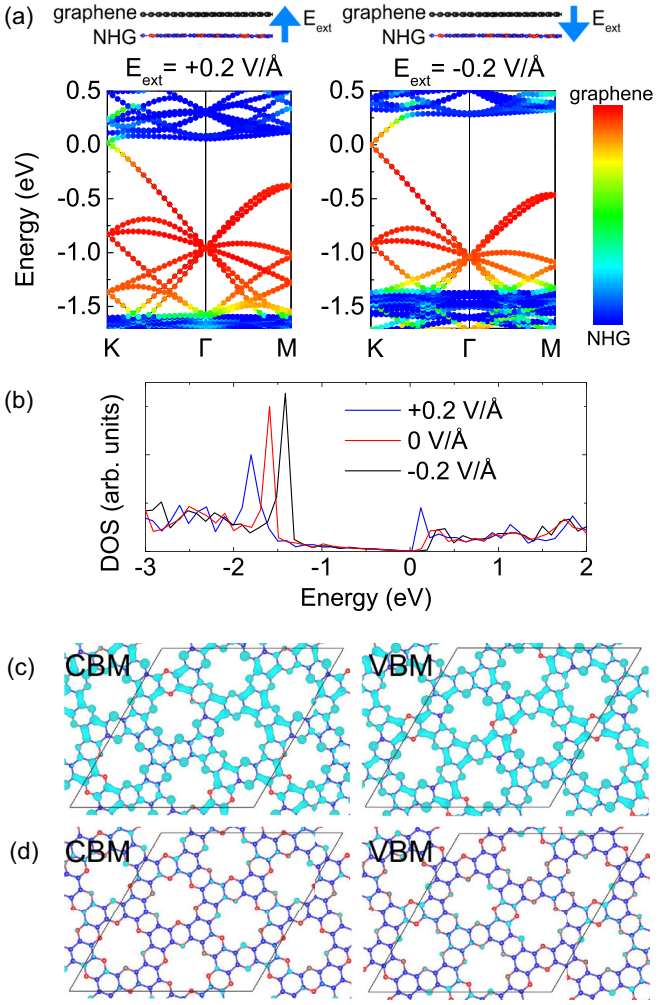

FIG. 5. (Color online) (a) Projected band structure of the (7,3)-(1,2) structure for two values of the external electric field. Blue and red color denotes the contribution from the NHG and graphene layers, respectively. Fermi level is set to zero. (b) The density of states (DOS) of the (7,3)-(1,2) structure with and without an electric field applied. Fermi level is zero. (c) The partial charge density of the VBM and CBM states at the K point for $E_{\text{ext}} = 0.2$ V/Å. Only the distribution on the NHG layer is shown. (d) The same as (b) but for $E_{\text{ext}} = -0.2$ V/Å. The isosurface corresponds to 0.00035 e/Å^3.

be considered to be intact. The linear band dispersion around the K point is also maintained. Compared with the case of zero field, for $E_{\text{ext}} = 0.2$ V/Å, the energy of the flat bands from the NHG layer [the blue dots in Fig. 5(a)] decreases, and for $E_{\text{ext}} = -0.2$ V/Å, these flat bands increase in energy. This happens because the electric field along $+z$ decreases the potential on the NHG side with respect to the graphene side, whereas the field along $-z$ increases the potential at the NHG side. Such an energy shift is also clear in the density of states plot in Fig. 5(b). As a result, the Dirac point becomes closer to (further from) the empty flat bands, and the interlayer hybridization for the states near the Fermi level becomes stronger (weaker) for E_{ext} along $+z$ ($-z$). Comparing Figs. 4(b), 5(c), and 5(d), it can be seen that the partial charge density of CBM and VBM in the NHG layer increases for positive E_{ext} and decreases for negative E_{ext}. Therefore, by applying an external field, the relative distribution of Dirac-fermion-like carriers over the two atomic layers can be tuned.

D. Renormalized Fermi velocity

Previous studies showed that when graphene is subject to a periodic potential, its Fermi velocity decreases [33,38]. In graphene heterostructures with moiré patterns, a periodic potential that follows the moiré pattern is created, thus the Fermi velocity of graphene is renormalized, as was shown in the case of twisted bilayer graphene [18,39]. In G/NHG heterostructures, because of the appearance of a moiré pattern, such renormalization is also expected. Figure 6(a) shows that the slope of the linear bands around the K points in the (7,3)-(1,2) structure is smaller than that in a pristine graphene monolayer. In other words, the Fermi velocity v_F of the (7,3)-(1,2) structure is reduced. Moreover, in graphene the v_F is the same for electrons and holes, and the calculated value is 8.46×10^5 m/s. However, the (7,3)-(1,2) structure exhibits electron-hole asymmetry. The calculated v_F is 6.24×10^5 m/s for holes and 6.02×10^5 m/s for electrons. Defining an asymmetry factor $\phi = 2(v_F(h) - v_F(e))/(v_F(h) + v_F(e))$, the asymmetry in the (7,3)-(1,2) structure is 3.6%.

In moiré pattern heterostructures, the relative angle θ between the layers can be arbitrary in principle. Different θ may result in different properties. For example, in bilayer graphene, the magnitude of the Fermi velocity renormalization depends on the relative twist angle [18,39]. A smaller angle leads to a larger moiré pattern and a stronger renormalization. To investigate moiré-patterned G/NHG heterostructures with different θ, we have performed TB calculations. The details of the TB model are described in the Appendix. Figure 6(a) also shows the band structure of the (7,3)-(1,2) G/NHG and graphene calculated by the tight-binding model, and the results agree well with those obtained from VASP. Here we consider different moiré patterned G/NHG with θ ranging from 0° to 30°, since $60° - \theta$ and θ create similar moiré patterns and they result in the same velocity renormalization. The interlayer spacing is fixed at 3.25 Å as in the (7,3)-(1,2) structure. In all structures studied, the lattice mismatch between graphene and NHG is less than 0.5%. The band gap opening at the Dirac point is always negligible. As shown in the inset of Fig. 6(c), its order of magnitude is 10^{-4} eV and decreases with decreasing twist angle. The linear band dispersion is well preserved in all structures. The band dispersion around the K point for several selected G/NHG heterostructures are shown in Fig. 6(b). Figure 6(c) presents the calculated Fermi velocity as a function of θ. The following results are found:

(i) There is always some electron-hole asymmetry in v_F. When θ is small, the asymmetry factor ϕ increases rapidly with decreasing θ, as show in the inset of Fig. 6(c). It reaches a maximum of 13% at $\theta = 0°$.

(ii) For $\theta > 15°$, v_F is almost independent of θ, but the value is only about 80% of that of pristine graphene, indicating that velocity renormalization occurs even for large θ. In bilayer graphene, when θ is large, the moiré pattern periodicity is small, and the pattern induced potential is almost uniform. As a result, the renormalization effect is weak [18,39]. However, the NHG has a special crystal structure, with large holes

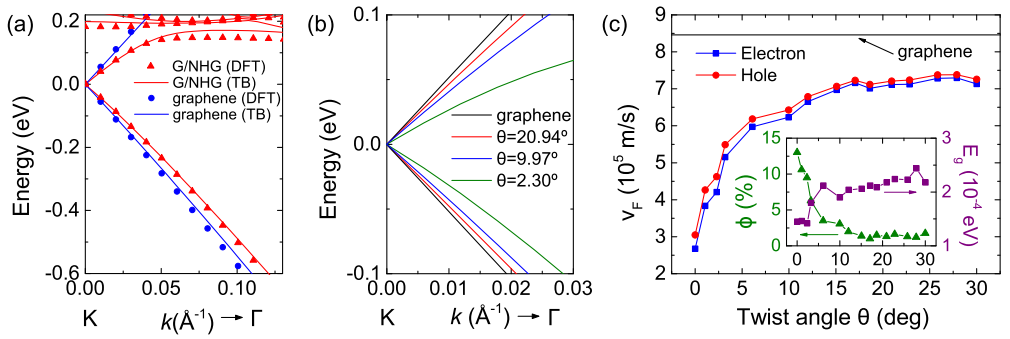

FIG. 6. (Color online) (a) Band dispersion of (7,3)-(1,2) G/NHG and graphene near the Fermi level calculated by DFT and TB. (b) Band dispersion of G/NHG with different twist angle θ around K. $\theta = 20.94^\circ$, 9.97°, and 2.30° correspond to (20,6)-(5,3), (8,15)-(0,6), and (20,1)-(3,4) stacking, respectively. (c) The calculated Fermi velocity v_F as a function of θ. Solid horizontal line indicates the value of pristine graphene. Inset: The electron-hole asymmetry factor ϕ of v_F and the band gap E_g at the Dirac point as a function of θ.

distributed periodically on the monolayer. The potential above the holes is very different from that above other regions. In the G/NHG heterostructures, these holes create nonuniform potentials with a periodicity of a_0^N, which is applied to the graphene layer. For large θ, although the size of the moiré pattern is small, the velocity renormalization is still significant due to the hole induced potentials.

(iii) For $\theta < 15^\circ$, v_F decreases when the angle decreases. It is known that bilayer graphene exhibits a similar behavior [18,39]. Moreover, for the graphene bilayer, in the case that θ is extremely small, the size of the moiré pattern becomes infinite because there is no lattice mismatch between the two graphene layers. This leads to a very strong velocity renormalization, and v_F is reduced to zero [18,27]. Such a behavior does not appear in the G/NHG heterostructure. When $\theta = 0^\circ$, v_F is reduced by a large extent but not to zero. It is about 30% of that of pristine graphene. Due to the lattice mismatch between graphene and NHG, even at $\theta = 0^\circ$, the moiré pattern size is still finite, with a periodicity of 86 Å. So v_F is not reduced to zero as in the graphene bilayer.

V. GRAPHENE ENCAPSULATED NHG

Finally we discuss the electronic properties of graphene encapsulated NHG (GENHG), namely a NHG layer sandwiched by two graphene layers. Here we consider a (7,3)-(1,2)-(7,3) GENHG, namely a (1,2) NHG layer is placed between two (7,3) graphene layers, as shown in Fig. 7(a). The interlayer distance is set to 3.25 Å. Note that in the case of GENHG, the moiré pattern is still preferred over other ordered stackings. In GENHG, there are two G/NHG heterostructures. It is a good approximation to estimate the interlayer binding energy in GENHG by adding up the binding energies of the two corresponding G/NHG structures. Based on the analysis in Sec. IV A, for GENHG, the ABA stacking can achieve a maximum binding energy of -33.04 meV/Å^2, but its strain energy is 8.99 meV/Å^2. The binding energy of (7,3)-(1,2)-(7,3) GENHG is -30.54 meV/Å^2, and its strain energy is almost zero. Similar to the case of G/NHG, the $E_b + E_s$ in the (7,3)-(1,2)-(7,3) GENHG is lower than in the ordered stacking configurations such as ABA, and a moiré pattern is favored.

The band structure of the (7,3)-(1,2)-(7,3) GENHG is calculated by the tight-binding model. The results are plotted in Fig. 7(b). The GENHG exhibits metallic character, and its band structure around the K point is much like the case of AA stacked bilayer graphene [40], which can be viewed as the overlap of two shifted linear spectra. Figure 7(c) shows the highest valence band around the K point of this system. While in the G/NHG heterostructure there is only one Dirac point at the K point, in the GENHG there is a ring at the Fermi level in which Dirac-fermion-like carriers are present around the K point. Distinct from AA stacked graphene, the inner and outer radial velocities of the states on this ring are very

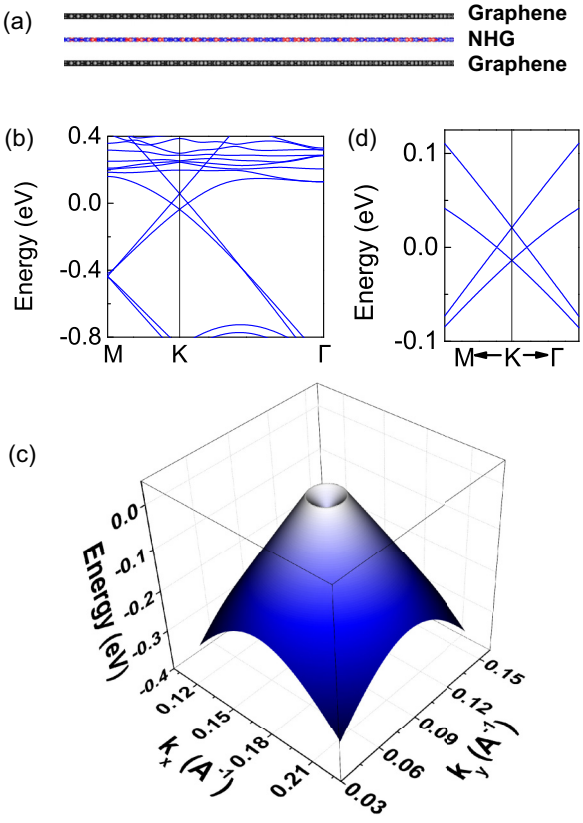

FIG. 7. (Color online) (a) Schematic of the GENHG structure. (b) Band dispersion and (c) the highest valence band around K of the (7,3)-(1,2)-(7,3) GENHG. (d) Band structure of (17,1)-(3,3)-(12,8) GENHG around the K point. The Fermi level is set to zero.

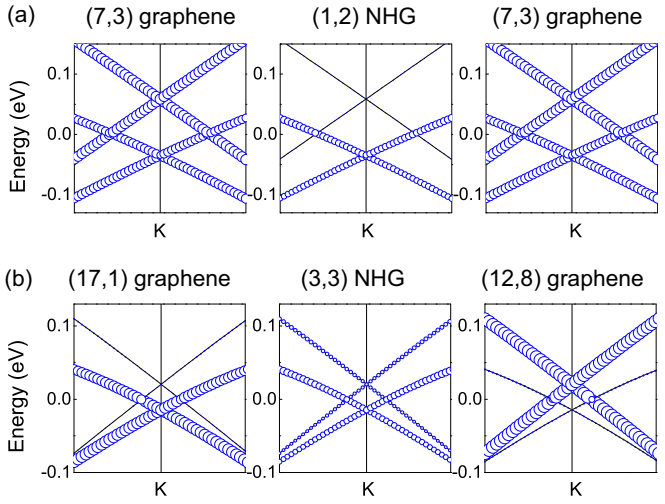

FIG. 8. (Color online) (a) The band structure of the (7,3)-(1,2)-(7,3) GENHG around the K point where the size of the circles is a measure of the contribution of the different layers to the carrier states. (b) The same as (a) but for the (17,1)-(3,3)-(12,8) GENHG.

different. Along the direction pointing to the K point, v_F is 4.94×10^5 m/s for electrons and 7.89×10^5 m/s for holes. Along the direction that is pointing away from the K point, v_F is 7.76×10^5 m/s for electrons and 4.69×10^5 m/s for holes. Note that in the present GENHG the two graphene layers have AA stacking. To see whether the presence of the "Dirac ring" depends on the stacking between the graphene layers, we have also calculated the band structure of a (17,1)-(3,3)-(12,8) GENHG, as shown in Fig. 7(d). Around the K point, the band structures is similar to the (7,3)-(1,2)-(7,3) GENHG. In the (17,1)-(3,3)-(12,8) GENHG, the two graphene layers are twisted with respected to each other and are no longer AA stacked. Therefore, the "Dirac ring" is a general feature in GENHG, which can be of potential interest for applications in high speed devices.

Here we propose a simple model for the possible origin of the Dirac ring. If one removes the NHG layer from the GENHG structure, the remaining two graphene layers can be viewed as two isolated ones since the distance between them is large. However, with the presence of the NHG layer in the middle, the interlayer coupling leads to relative energy shift between the two Dirac cones. As a result, the conduction band of the lower Dirac cone overlaps with the valence band of the upper Dirac cone, leading to the formation of a Dirac ring. To further confirm this prediction, we calculated the projected weights of the carrier states of the two graphene layers and the NHG layer in the band structure of the (7,3)-(1,2)-(7,3) and (17,1)-(3,3)-(12,8) GENHG, which is shown in Fig. 8. Interestingly different behaviors are observed in the two structures. In the (7,3)-(1,2)-(7,3) GENHG, the two Dirac cones have contributions from both graphene layers. However, the NHG layer only couples to the lower Dirac cone. This can be attributed to the symmetry of the wave functions at these two Dirac cones. Because the two graphene layers are AA stacked, the system has mirror symmetry and the NHG layer is the mirror plane. Therefore, the wave function of each eigenstate has a definite parity with respect to the mirror plane, either odd or even. Because of the p_z orbital character, the parity of the wave function of the NHG layer is always odd. That is to say, the NHG layer can only have contributions to the states with odd parity, and its coupling to even-parity states is symmetry forbidden. We found that the states corresponding to the lower Dirac cone in Fig. 8 have odd parity while those belonging to the upper Dirac cone have even parity. The NHG layer only couples to the former and changes its energy, but not to the latter. This leads to the proposed energy shift between the Dirac cones and thus the formation of the Dirac ring. The situation is different in the (17,1)-(3,3)-(12,8) GENHG. Figure 8(b) reveals that the upper Dirac cone comes from the (12,8) graphene layer, while the lower Dirac cone comes from the (17,1) graphene layer. There is no mirror symmetry in this structure, so the NHG layer can couple to both Dirac cones. However, as seen in the middle panel of Fig. 8(b), the coupling strength to the lower Dirac cone is stronger than that to the upper Dirac cone. This happens because the twist angle in (17,1)-(3,3) G/NHG is smaller than that in (12,8)-(3,3) G/NHG. As discussed in Sec. IV D, a smaller twist angle leads to a stronger interlayer coupling. The different coupling strength results in a relative energy shift of the two Dirac cones and leads to the formation of a Dirac ring.

VI. CONCLUSION

The structural and electronic properties of heterostructures of graphene and NHG were studied using first-principles and tight-binding calculations. It is demonstrated that a moiré pattern is favorable in the G/NHG heterostructure, instead of the lattice-coherent structure, because of the large strain energy in the latter. In moiré-patterned G/NHG, the band gap opening at the K point is negligible, and the linear band dispersion of graphene is well maintained. Due to the interlayer coupling, the VBM and CBM states have significant contributions from the NHG layer. By applying an electric field along the $+z$ or $-z$ direction, the coupling strength can be either enhanced or weakened. Fermi velocity renormalization is observed in the G/NHG heterostructures. When the twist angle θ between graphene and NHG is larger than 15°, v_F in the heterostructure does not change with θ, but the value is reduced to 80% of that of pristine graphene due to the holely structure of NHG. When θ is smaller than 15°, v_F decreases rapidly with decreasing θ. The heterostructures also exhibit electron-hole asymmetry in v_F, which is enhanced for small θ. The GENHG shows an interesting band structure near the Fermi level, much like the overlap of two shifted linear spectra. As a result, a "Dirac ring" around the K point appears in the Brillouin zone at the Fermi level. Its presence is robust with respect to the relative stacking of the two graphene layers. The preserved Dirac-fermion

TABLE I. The parameters used when calculating the different $V_{pp\pi}$ and $V_{pp\sigma}$.

	$V_{pp\sigma}^{\text{C1-C2}}$	$V_{pp\sigma}^{\text{C1-N}}$	$V_{pp\pi}^{\text{C1-C1}}$	$V_{pp\pi}^{\text{C2-C2}}$	$V_{pp\pi}^{\text{C2-N}}$	$V_{pp\pi}^{\text{N-N}}$
γ (eV)	0.48	0.48	−2.70	−2.70	−2.70	−2.70
a (Å)	3.250	3.250	1.418	1.460	1.335	1.335
q	2.218	5.518	2.218	2.218	5.518	5.518

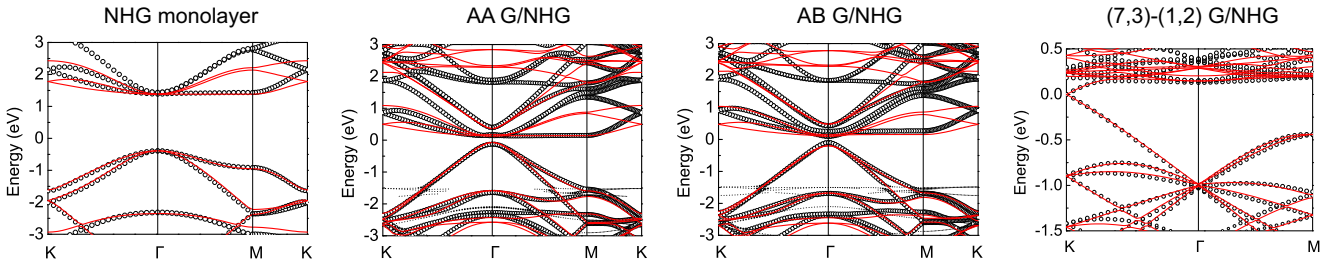

FIG. 9. (Color online) Comparison between the p_z band structures of different structures calculated by VASP (circles) and the TB model (red lines).

character and its electronic field tunability will be an asset for future applications of such G/NHG heterostructures in field effect devices.

ACKNOWLEDGMENTS

This work was supported by the Flemish Science Foundation (FWO-Vl) and the Methusalem foundation of the Flemish government. Computational resources were provided by TUBITAK ULAKBIM, High Performance and Grid Computing Center (TR-Grid e-Infrastructure), and HPC infrastructure of the University of Antwerp (CalcUA). J.K. is supported by a FWO Pegasus Short Marie Curie Fellowship.

APPENDIX: TIGHT-BINDING MODEL FOR GRAPHENE/NHG

The tight-binding Hamiltonian and the coupling parameter are given in Eqs. (1) and (2) in Sec. II. When r_{ij} is large the orbital coupling becomes negligible, thus a cutoff radius $r_{\rm cut}$ can be introduced. For $r_{ij} > r_{\rm cut}$, t_{ij} is considered to be zero. For $r_{ij} < r_{\rm cut}$, $V_{pp\pi}$ and $V_{pp\sigma}$ are calculated using the same expression $\gamma e^{q(1-r_{ij}/a)}$ but with different parameters γ, q, and a. These parameters, as well as the ϵ_i, can be tuned to reproduce the *ab initio* band structure. ϵ_i depends on the type of the atom at $\vec{r}_i$, and $V_{pp\pi}$ and $V_{pp\sigma}$ depend on the type of the atoms at $\vec{r}_i$ and $\vec{r}_j$. When the type of atoms change, the corresponding parameters can also be different. In the graphene/NHG heterostructure, there are three types of atoms: C1 (C atoms in the graphene layer), C2 (C atoms in the NHG layer), and N. For the onsite energy ϵ_i, the relative value between the different types is important. Adding a constant to all ϵ_i doesn't change the band dispersion and only results in a rigid shift of the band structure. In our calculations, taking the onsite energy of C1 as zero, the onsite energy of C2 and N are -0.27 eV and -0.70 eV, respectively. For each heterostructure, a constant energy shift is added to all the onsite energies to make the energy of the Dirac point zero. The parameters used for calculating the different $V_{pp\pi}$ and $V_{pp\sigma}$ are listed in Table I. The cutoff radius $r_{\rm cut}$ is chosen as 6 Å, which is sufficient to obtain converged results.

In Fig. 9 the p_z band structures of different structures calculated by VASP and the TB model are presented. It can be seen that the TB results agree with the VASP results quite well, especially around the Fermi level, indicating the validity of the TB model.

[1] K. S. Novoselov, A. K. Geim, S. V. Morozov, D. Jiang, Y. Zhang, S. V. Dubonos, I. V. Grigorieva, and A. A. Firsov, Science **306**, 666 (2004).
[2] A. K. Geim and K. S. Novoselov, Nat. Mater. **6**, 183 (2007).
[3] J. Lahiri, Y. Lin, P. Bozkurt, I. I. Oleynik, and M. Batzill, Nat. Nanotechnol. **5**, 326 (2010).
[4] J. Bai, X. Zhong, S. Jiang, Y. Huang, and X. Duan, Nat. Nanotechnol. **5**, 190 (2010).
[5] H. Şahin and S. Ciraci, Phys. Rev. B **84**, 035452 (2011).
[6] E. L. Spitler and W. R. Dichtel, Nat. Chem. **2**, 672 (2010).
[7] J. W. Colson and W. R. Dichtel, Nat. Chem. **5**, 453 (2013).
[8] A. P. Cote, A. I. Benin, N. W. Ockwig, M. O'Keeffe, A. J. Matzger, and O. M. Yaghi, Science **310**, 1166 (2005).
[9] S. Kandambeth, D. B. Shinde, M. K. Panda, B. Lukose, T. Heine, and R. Banerjee, Angew. Chem., Int. Ed. **52**, 13052 (2013).
[10] J. Mahmood, E. K. Lee, M. Jung, D. Shin, I.-Y. Jeon, S.-M. Jung, H.-J. Choi, J.-M. Seo, S.-Y. Bae, S.-D. Sohn, N. Park, J. H. Oh, H.-J. Shin, and J.-B. Baek, Nat. Commun. **6**, 6486 (2015).
[11] B. Xu, H. Xiang, Q. Wei, J. Liu, Y. Xia, J. Yin, and Z. Liu, Phys. Chem. Chem. Phys. **17**, 15115 (2015).
[12] J. Mahmood, S.-M. Jung, S.-J. Kim, J. Park, J.-W. Yoo, and J.-B. Baek, Chem. Mater. **27**, 4860 (2015).
[13] R. Zhang and J. Yang, arXiv:1505.02768.
[14] A. K. Geim and I. V. Grigorieva, Nature (London) **499**, 419 (2013).
[15] P. Rivera, J. R. Schaibley, A. M. Jones, J. S. Ross, S. Wu, G. Aivazian, P. Klement, K. Seyler, G. Clark, N. J. Ghimire, J. Yan, D. G. Mandrus, W. Yao, and X. Xu, Nat. Commun. **6**, 6242 (2015).
[16] C.-H. Lee, G.-H. Lee, A. M. van Der Zande, W. Chen, Y. Li, M. Han, X. Cui, G. Arefe, C. Nuckolls, T. F. Heinz, J. Guo, J. Hone, and P. Kim, Nat. Nanotechnol. **9**, 676 (2014).
[17] F. Withers, O. Del Pozo-Zamudio, A. Mishchenko, A. P. Rooney, A. Gholinia, K. Watanabe, T. Taniguchi, S. J. Haigh, A. K. Geim, A. I. Tartakovskii, and K. S. Novoselov, Nat. Mater. **14**, 301 (2015).
[18] G. Trambly de Laissardière, D. Mayou, and L. Magaud, Nano Lett. **10**, 804 (2010).

[19] L. Ponomarenko, R. V. Gorbachev, G. L. Yu, D. C. Elias, R. Jalil, A. A. Patel, A. Mishchenko, A. S. Mayorov, C. R. Woods, J. R.Wallbank, M. Mucha-Kruczynski, B. A. Piot, M. Potemski, I. Grigorieva, K. S. Novoselov, F. Guinea, V. I. Falko, and A. K. Geim, Nature (London) **497**, 594 (2013).
[20] P. E. Blöchl, Phys. Rev. B **50**, 17953 (1994).
[21] G. Kresse and J. Hafner, Phys. Rev. B **47**, 558 (1993).
[22] G. Kresse and J. Furthmüller, Phys. Rev. B **54**, 11169 (1996).
[23] J. P. Perdew, K. Burke, and M. Ernzerhof, Phys. Rev. Lett. **77**, 3865 (1996).
[24] R. F. W. Bader, *Atoms in Molecules - A Quantum Theory* (Oxford University Press, Oxford, 1990).
[25] G. Henkelman, A. Arnaldsson, and H. Jónsson, Comput. Mater. Sci. **36**, 354 (2006).
[26] S. Grimme, J. Comput. Chem. **27**, 1787 (2006).
[27] G. Trambly de Laissardière, D. Mayou, and L. Magaud, Phys. Rev. B **86**, 125413 (2012).
[28] J. C. Slater and G. F. Koster, Phys. Rev. **94**, 1498 (1954).
[29] R. Zhang, B. Li, and J. Yang, Nanoscale **7**, 14062 (2015).
[30] W. Yang, G. Chen, Z. Shi, C.-C. Liu, L. Zhang, G. Xie, M. Cheng, D. Wang, R. Yang, D. Shi, K. Watanabe, T. Taniguchi, Y. Yao, Y. Zhang, and G. Zhang, Nat. Mater. **12**, 792 (2013).
[31] M. Neek-Amal and F. M. Peeters, Phys. Rev. B **82**, 085432 (2010).
[32] B. Sachs, T. O. Wehling, M. I. Katsnelson, and A. I. Lichtenstein, Phys. Rev. B **84**, 195414 (2011).
[33] C.-H. Park, L. Yang, Y.-W. Son, M. L. Cohen, and S. G. Louie, Nat. Phys. **4**, 213 (2008).
[34] Y. Fan, M. Zhao, Z. Wang, X. Zhang, and H. Zhang, Appl. Phys. Lett. **98**, 083103 (2011).
[35] X. Zhong, Y. K. Yap, R. Pandey, and S. P. Karna, Phys. Rev. B **83**, 193403 (2011).
[36] J. Xue, J. Sanchez-Yamagishi, D. Bulmash, P. Jacquod, A. Deshpande, K. Watanabe, T. Taniguchi, P. Jarillo-Herrero, and B. J. LeRoy, Nat. Mater. **10**, 282 (2011).
[37] E. V. Castro, K. S. Novoselov, S. V. Morozov, N. M. R. Peres, J. M. B. Lopes dos Santos, J. Nilsson, F. Guinea, A. K. Geim, and A. H. Castro Neto, Phys. Rev. Lett. **99**, 216802 (2007).
[38] M. Barbier, P. Vasilopoulos, and F. M. Peeters, Phys. Rev. B **81**, 075438 (2010).
[39] A. Luican, G. Li, A. Reina, J. Kong, R. R. Nair, K. S. Novoselov, A. K. Geim, and E. Y. Andrei, Phys. Rev. Lett. **106**, 126802 (2011).
[40] I. Lobato and B. Partoens, Phys. Rev. B **83**, 165429 (2011).